Visible Light Photocatalyst: Iodine-Doped Mesoporous Titania with a Bicrystalline Framework

Gang Liu,[†] Zhigang Chen,[†] Chunlei Dong,[†] Yanning Zhao,[†] Feng Li,[†] Gao Qing Lu,*[,‡] and Hui-Ming Cheng*[,†]

Shenyang National Laboratory for Materials Science, Institute of Metal Research, Chinese Academy of Sciences, 72 Wenhua Road, Shenyang 110016, China, and Australian Research Council Centre for Functional Nanomaterials, School of Engineering, The University of Queensland, Queensland 4072, Australia

Iodine-doped (I-doped) mesoporous titania with a bicrystalline (anatase and rutile) framework was synthesized by a two-step template hydrothermal synthesis route. I-doped titania with anatase structure was also synthesized without the use of a block copolymer as a template. The resultant titania samples were characterized by X-ray diffraction, Raman spectroscopy, Fourier transform infrared, nitrogen adsorption, transmission electron microscopy, X-ray photoelectron spectroscopy, and UV−visible absorption spectroscopy. Both I-doped titania samples, with and without template, show much better photocatalytic activity than commercial P25 titania in the photodegradation of methylene blue under the irradiation of visible light (>420 nm) and UV−visible light. Furthermore, I-doped mesoporous titania with a bicrystalline framework exhibits better activity than I-doped titania with anatase structure. The effect of rutile phase in titania on the adsorptive capacity of water and surface hydroxyl, and photocatalytic activity was investigated in detail. The excellent performance of I-doped mesoporous titania under both visible light and UV−visible light can be attributed to the combined effects of bicrystalline framework, high crystallinity, large surface area, mesoporous structure, and high visible light absorption induced by I-doping.

1. Introduction

Photocatalysis has attracted worldwide research interest because of its potential in utilization of solar energy in the past decades. Titania as one of the most promising photocatalysts has been widely investigated for its attractive applications in water splitting and mineralization of toxic organic substances.[1−3] Many advantages such as high efficiency, good stability, ready availability, and nontoxicity exist for titania-based photocatalysts. However, a fatal disadvantage for the titania photocatalyst is its large band gap (3.2 and 3.0 eV for anatase and rutile, respectively), which makes titania absorb only UV light. So its application is constrained to only the UV light range. To extend its application into the dominant visible light range in solar light, many efforts have been made and challenges do exist in finding a new material system that can effectively utilize the visible light irradiation.

To achieve efficient photocatalysis in the visible light range, one strategy is to reduce the band gap of titania. Substitutional doping as an effective method is widely used to change the electron structure of the matrix. In doping of titania, both cation and anion can be replaced with proper elements by wet chemical methods and physical methods. Anion doping has shown a great potential in improving the photocatalytic activity of titania in the visible light range because it can reduce the band gap by forming doping levels in the band gap.[4] Many works have been conducted to develop visible light photocatalyst $TiO_{2−X}A_X$ (A = N, C, and F)[4−7] and nonmetal cation doping (C, S, I, and

P)[8−11] has also been reported. On the other hand, many works[12−14] have focused on the synthesis of nanocrystalline titania with mesoporous structure, which exhibits a great potential in further improving photocatalytic activity because of its abundant pores and large surface area. Metal cation doped mesoporous titania[15−18] was also developed; however, little attention has been paid to the formation of mesoporous structure of anion and nonmetal cation doped titania.[19,20] It is thought that mesoporous structure with its unique structural characteristics can also be useful for the improvement of photocatlaytic activity of anion and nonmetal cation doped titania. Here, we report I-doped mesoporous titania (denoted as MTI) with a bicrystalline framework as active visible light photocatalyst by a two-step hydrothermal template synthesis route. The resultant photocatalyst shows much better photocatalytic activity than I-doped titania (denoted as TI) with anatase structure.

2. Experimental Methods

2.1. Sample Preparation. Ti[OCH(CH₃)₂]₄ (7 mL, Aldrich, 97%) dissolved in 40 mL of isopropyl alcohol was dropwise added to 60 mL of distilled water with 3 g of iodic acid dissolved in it. After continuous stirring of the reaction mixture for 5 h, hydrothermal treatment in a Teflon-lined autoclave was applied to the resultant suspension at 80 °C for 4 h to obtain seed solution. The block copolymer Pluronic P123 (Aldrich), denoted as $EO_{20}PO_{70}EO_{20}$, was used as the template for the second step. P123 (2.5 g) was dissolved in 40 mL of distilled water. The seed solution cooled to 45 °C around was dropwise added into the P123 solution at 45 °C under stirring. The mixture was stirred at constant temperature 45 °C for 2 h so that the formed micelles can fully act with the seeds. Then the mixture was transferred into Teflon-lined autoclave for thermal treatment at

---

* To whom correspondence should be addressed. E-mail: maxlu@uq.edu.au (Prof. Max Lu); cheng@imr.ac.cn (Prof. Hui-Ming Cheng).
† Shenyang National Laboratory for Materials Science.
‡ Australian Research Council Centre for Functional Nanomaterials.

TABLE 1: Physicochemical Properties of the Prepared TI and MTI in Comparison with Those of P25

	anatase		rutile				
	crystal size (nm)	content (%)	crystal size (nm)	content (%)	S_{BET} (m²/ g)	pore size (nm)	pore volume (cm³/g)
P25	36	81	88	19	51		0.165
TI	9	100		0	118	9.9	0.298
MTI	10	57	16	43	157	6	0.248

100 °C for 20 h. The resultant powder was recovered by using evaporation at 60 °C before calcination in a muffle furnace at 400 °C for 2 h. The sample was denoted as MTI.

I-doped anatase titania as a reference sample, denoted as TI, was synthesized according to Hong et al.[10] and Ti[OCH(CH₃)₂]₄ instead of tetrabutyl titanate was used as precursor.

2.2. Characterization. X-ray diffraction (XRD) patterns were recorded on Rigaku diffractometer using Cu irradiation. Transmission electron microscopy (TEM) images were performed on JEOL 2010 electron microcopy instrument. The Brunauer−Emmett−Teller (BET) surface area and pore size distribution were determined by nitrogen adsorption−desorption isotherm measurements at 77 K (ASAP 2010). The binding energy was identified by X-ray photoelectron spectroscopy with Mg Kα radiation (PHI5300). A UV−vis spectrophotometer (JASCO-V550) was used to obtain the optical absorbance spectra of the samples. Raman and Fourier transform infrared (FTIR) spectra were recorded on LabRam HR 800 and Matna-IR 560, respectively. In the measurement of IR spectra, the samples were mixed with KBr and the concentration of the samples was kept around 0.3% in weight.

2.3. Measurement of Photocatalytic Activity. The photocatalytic experiments were carried out by adding 100 mg of titania samples into 100 mL of 2×10^{-5} M methylene blue (MB) solution. The suspension was stirred in dark for 30 min to obtain the saturated adsorption of MB before illumination. The light source used was a fluorescence lamp (LS-2000, 18 W).

Figure 1. XRD spectra of MTI with a bicrystalline framework and TI with anatase structure.

Figure 2. XRD spectra of samples at different stages. (1) Anatase seeds after the first-step hydrothermal treatment, (2) titania after calcination of anatase seeds at 400 °C for 2 h in air, (3) product after the second-step treatment, and (4) sample MTI.

A long-pass glass filter with 420 nm was employed to evaluate the photocatalytic activity in visible light range.

3. Results and Discussion

3.1. Formation of Bicrystalline Phase. Figure 1 shows XRD spectra of the prepared samples MTI and TI. The crystal size of the resultant titania nanoparticles is determined by Scherrer's equation

$$D = 0.89\lambda/\beta \cos \theta \qquad (1)$$

where D is the crystal size, λ is the wavelength of X-ray radiation, β is the full width at half-maximum, and θ is the diffraction angle. The phase contents of titania are obtained from the following formulas[21]

$$W_R = 1/(1 + 0.8I_A/I_R) \qquad (2)$$

$$W_A = 1 - W_R \qquad (3)$$

where W_R and W_A are the content of rutile and anatase titania, respectively, I_A and I_R represent the diffraction intensities of anatase (101) and rutile (110). The crystal sizes and phase contents of anatase and rutile titania are shown in Table 1.

From the XRD patterns, it was found that a bicrystalline structure appears in I-doped mesoporous titania (MTI) by the two-step template hydrothermal synthesis route. In our previous work,[22] both strong acid (hydrochloric acid) and neutral routes were employed to synthesize mesoporous titania for photoelectrochemical solar cells. In the strong acid synthesis route, a certain rutile appeared in the dominant anatase titania but no rutile was detected in the neutral route. In our current synthesis route, the first-step hydrothermal treatment leads to the formation of the absolutely pure anatase seeds, proved by the pure anatase structure after calcination of anatase seeds at 400 °C for 2 h in air (shown in Figure 2). However, the bicrystalline structure is obtained after calcination of the second-step hydrothermal product at 400 °C for 2 h in air. It has demonstrated that rutile phase cannot be formed by calcinating at 400 °C. So rutile phase in the bicrystalline titania was formed in the second-step hydrothermal treatment. To confirm the role of HIO₃ in the phase transformation, we also conducted the experiments by increasing different amount of HIO₃ in neutral water and decreasing the pH value with nitric acid at the same level of HIO₃. It was found that the content of rutile titania increased with the increase of HIO₃ and nitric acid. So rutile phase as the most stable phase of titania is strong acid dependent under hydrothermal treatment. One reason for this can be that the protonation to the surface of anatase seeds lowers the activation energy for the rutile formation by partially blocking the anatase growth.[22] Under our synthesis conditions, the second-step was maintained at 100 °C for 20 h so iodic acid as a weak acid can have a full hydrolization and supply a strong acidity at 100 °C synthesis condition.

Nitrogen adsorption−desorption isotherms and pore size distribution of the resultant samples are shown in Figure 3. For both samples, type IV isotherms are observed, which is characteristic of mesoporous materials.[23] From the isotherms, it can
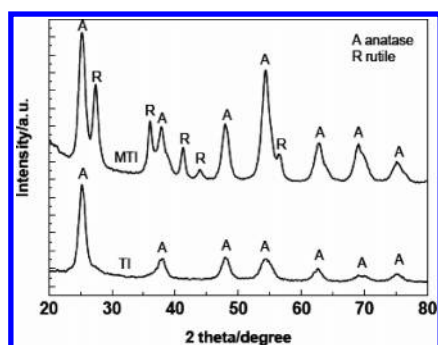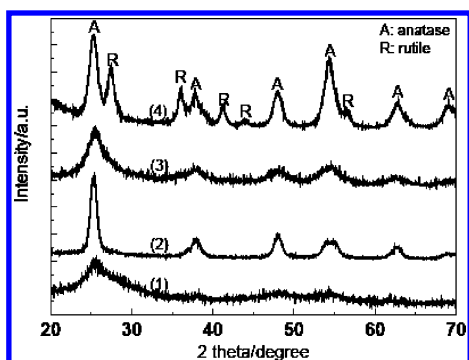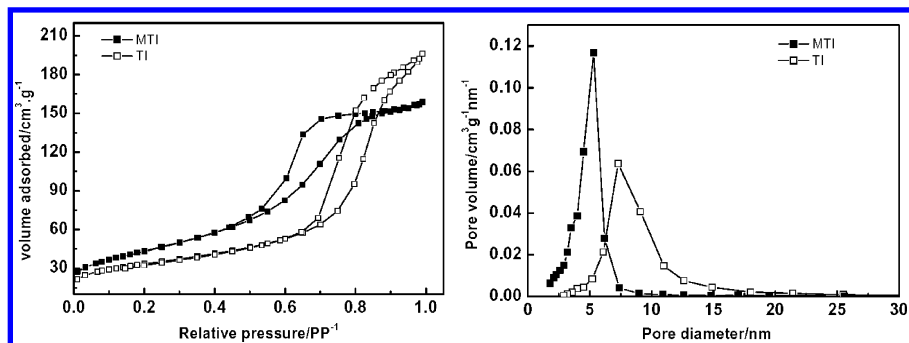
Visible Light Photocatalyst

J. Phys. Chem. B, Vol. 110, No. 42, 2006 **20825**

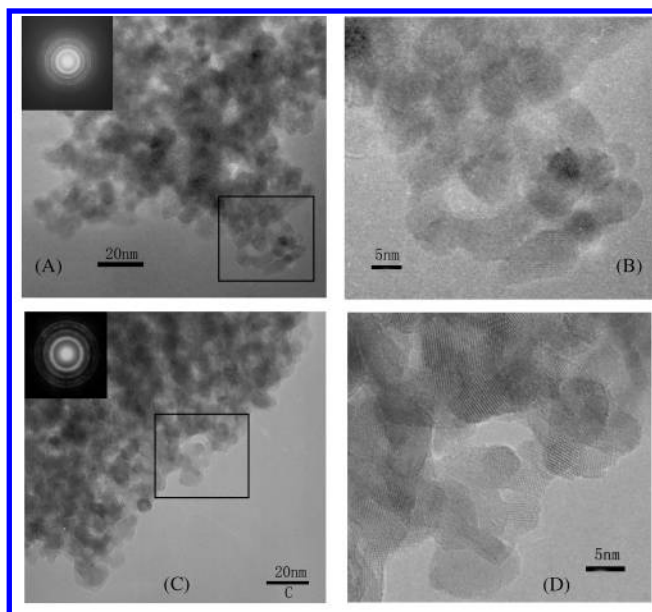**Figure 3.** Nitrogen adsorption−desorption isotherm and pore size distribution of TI and MTI.

Figure 4. TEM images of the samples TI (A) and MTI (C). Images B and D are the area bound by the rectangle in A and B, respectively.

Figure 5. IR spectra of the samples P25, TI, and MTI. (a) As-prepared samples, and (b) the samples treated at 110 °C in a vacuum for 24 h.

be seen that the monolayer adsorption is complete when the relative pressure reaches 0.5 for sample MTI. However, the monolayer adsorption for TI is not complete until reaching a relative pressure of 0.65. This indicates that sample MTI possesses much smaller pore size than sample TI. The BJH analysis of pore size distribution from the desorption branch of isotherm also demonstrates that the pore size of sample MTI is smaller. Furthermore, the pore size distribution for MTI with a full width at half maximum (fwhm) value of 1.466 is much narrower than the sample TI with fwhm of 3.301.

The BET surface area, pore size, and volume of titania samples are also shown in Table 1. It can be seen that the sample MTI possesses a smaller pore size with high porosity and large surface area. The pores in MTI originate from the previously occupied space by the block copolymer micelle, as suggested by our previous work.[22] The removal of the block copolymer micelle as template brings about the formation of pores with narrow size distribution, as demonstrated by TEM images (parts C and D of Figure 4). The wormholelike interstitial pores with irregular structure were observed. For sample TI, the pores are presumably formed by the aggregation of small particles when calcination at 400 °C was performed during preparation. In this case, the pores can be random due to the lack of template to tailor the pore. So the pore size distribution from 2 to 20 nm is much broader than sample MTI, in which the pore size can be tailored by the block copolymer micelle as the template. The TEM images in parts A and B of Figure 4 also demonstrate the heterogeneity of pore sizes.
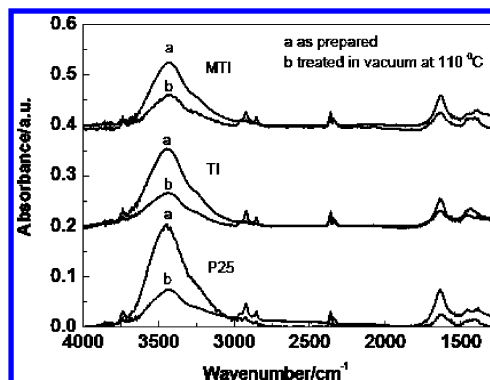
3.2. FTIR Spectroscopy. FTIR spectra are collected to study the surface chemistry of the photocatalysts under two conditions. Figure 5 compares the IR absorbance spectra for samples P25, TI, and MTI, which contain different rutile contents. It is interesting to see the absorbance bands around 3400 and 1650 cm^{-1} (Figure 5) originated from surface adsorbed water and surface hydroxyl,[24] which is traditionally recognized as an important factor affecting the photocatalytic activity.[24,25] The greater the number of surface hydroxyl, the faster the photocatalytic reaction.[26] It can be seen that the peak intensities of surface adsorbed water and surface hydroxyl groups for both TI and MTI are marginally lower than that of P25. Interestingly, the intensity of surface adsorbed water and surface hydroxyl groups for sample MTI with 43% rutile phase is comparable to sample TI with absolutely pure anatase phase. It seems that the existence of rutile in titania has not decreased the amount of adsorbed water and hydroxyl groups. This trend is different from the previous result: anatase is more active than rutile in adsorbing water and hydroxyl groups.[24] Crystal size and particle size for samples MTI and TI are nearly the same and surface area for MTI is larger than TI (in Table 1). So it means that rutile phase can also be active in adsorbing water and hydroxyl groups when rutile titania possesses similar crystal size, particle size, and surface area as compared to anatase titania.

3.3. Raman Spectroscopy. Compared to XRD, Raman spectroscopy is a much more sensitive technique for the detection of nanosized crystalline domain.[27] XRD is a powerful tool to determine the period crystal structure with a long range, but its detection limit (up to 5 mol %) is relatively high. Raman spectroscopy is sensitive to some vibration modes (Raman active modes) in crystal structure. So it is useful to characterize local surface structure. For nanosized particles, its period structure is greatly limited due to the small size. In addition, doping can also modify surface structure of matrix, which is not easy to be detected by X-ray diffraction. In this case, more detailed information can be derived from Raman spectra. Figure 6 shows
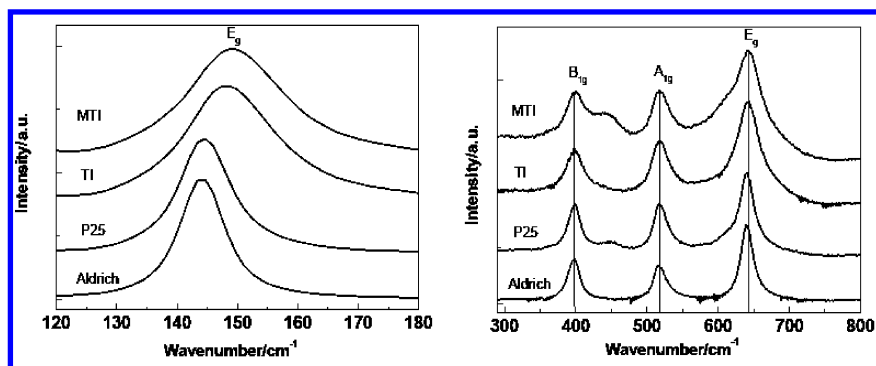
Figure 6. Raman spectra of MTI, TI, commercial P25, and anatase titania from Aldrich.

TABLE 2: Wavenumber of the Raman Spectra of Samples MTI, TI, P25, and Anatase Titania from Aldrich (cm^{-1})

	E_g	E_g	B_{1g}	A_{1g}	E_g
Aldrich	144	196	397	519	640
P25	144	196	397	519	640
TI	148	196	397	519	642
MTI	149	196	397	519	642

Raman spectra of two samples (TI and MTI) and two commercial samples (Aldrich, pure anatase with crystal size larger than 100 nm; P25, anatase and rutile) selected as references. For anatase, there are six Raman active modes ($3E_g + 2B_{1g} + A_{1g}$). Four Raman active modes ($B_{1g} + E_g + A_{1g} + B_{2g}$) can be assigned to rutile titania. Raman modes observed in the single-crystal anatase titania are 144 (E_g), 197 (E_g), 399 (B_{1g}), 513 (A_{1g}), 519 (B_{1g}), and 639 cm^{-1} (E_g).[28] Raman active modes for each sample are shown in Table 2. The main features of the spectra of samples TI and MTI are similar to the references P25 and pure anatase titania from Aldrich. There are two shoulders between 400 and 500 cm^{-1} and 600 and 630 cm^{-1} for the spectra of MTI and P25, which are assigned to the vibrational modes of the rutile phase. Compared to P25 and Aldrich samples, there is a notable shift to higher wavenumbers for the two Raman peaks of TI and MTI samples, E_g modes at 144 and 640 cm^{-1}. Meanwhile, the Raman peaks are much broader for I-doped nanocrystal titania, TI and MTI. To understand the shift and broadening of Raman peaks, two factors including size effect and doping should be considered. The crystal size of samples TI and MTI is much smaller than that of P25 and anatase titania from Aldrich. The effect of grain size on the mode shift and broadening in the spectra of titania nanoparticles has been observed,[29] and it was suggested that the shift in the Raman spectra of titania could be caused by the effect of smaller particle size on the force constants and vibrational amplitudes of the nearest neighbors.[29] The broadening might be attributed to the finite lifetime of the vibrational modes in the smaller size nanoparticles.[30] On the other hand, iodine doping can destroy the symmetry of Ti−O−Ti network, to some extent. The change in symmetry can affect some vibration modes, and then cause the shift of certain Raman modes.

3.4. XPS Analysis and Optical Properties. XPS spectra (Figure 7) for samples TI and MTI show the similarity in the values for binding energy of I3d5. The similar binding energy in both samples means the same state of doped iodine. The contents of I in samples TI and MTI were found to be 4.6 and 5.2 atomic %, respectively. The binding energy of I3d5 observed at 624.5 eV for samples TI and MTI is higher than that of HIO$_3$ (623 eV), but it is much smaller than the result of 627.5 eV reported by Hong et al.[10] As it is known, electrons in the inner orbital are attracted by atomic nucleus and also repulsed by outer electrons. The decrease in the density of outer electrons will
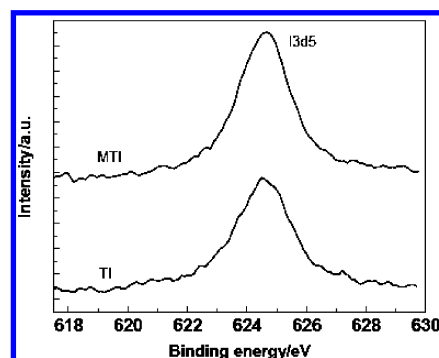

Figure 7. I3d5 XPS spectra of MTI and TI.

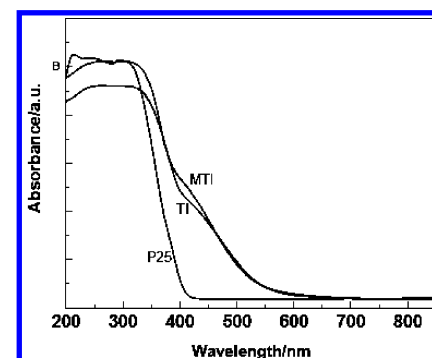**Figure 8.** 8. Optical absorbance spectra of P25, MTI, and TI.

lead to the increase of binding energy. This is the reason that high valence state possesses high binding energy. For I-doped titania, the binding energy of doped I in titania matrix is larger than that of I in HIO$_3$. It can be inferred that the oxidation state of doped I should be higher than that of I in HIO$_3$, to some extent. However, it is very difficult to determine the exact oxidation state of doped I in titania matrix due to the redistribution of outer electrons. On the other hand, ionic radii for Ti^{4+} and I^{5+} are 0.68 and 0.94 Å, and covalent radii for transition metal titanium and iodine are 1.32 and 1.33 Å, respectively. Since the degree of ionicity for transition metal oxide TiO$_2$ is intermediate between fully ionic and fully covalent, the actual radius for the Ti^{4+} in TiO$_2$ should be between 0.68 and 1.32 Å. The replacement of Ti^{4+} with I in a TiO$_2$ matrix will also increase ionicity of I compared to I in HIO$_3$. Accordingly, the radius of the doped I in titania matrix should be between 0.94 and 1.33 Å. From the view of radius matching, it is possible for the substitution of I for Ti^{4+} in titania matrix.

Figure 8 shows the optical absorbance spectra for P25 (Degussa), samples TI and MTI. The synthesized samples TI and MTI demonstrate an obvious absorption in the visible light range from 400 to 550 nm, which is consistent with the yellow
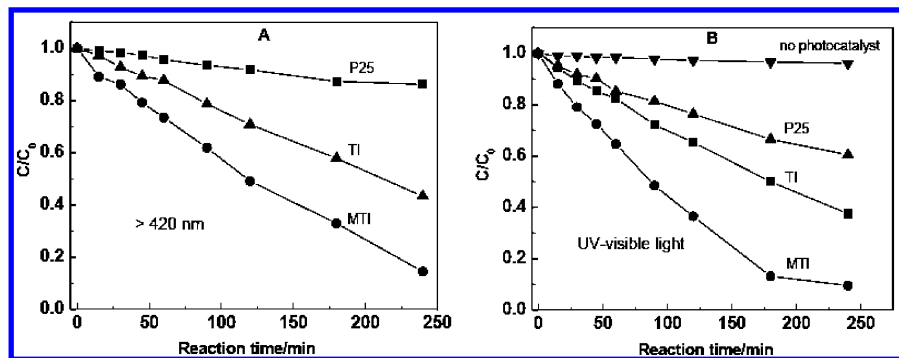
Figure 9. MB photodegradation of the samples MTI, TI, and P25 under visible light ($\lambda > 420$ nm) and UV−visible light irradiation, respectively.

color of the samples. The high absorption in the visible light range is definitely attributed to iodine doping.

3.5. Photocatalytic Activity. To compare the photocatalytic activity of commercial titania (P25), TI and MTI, photodegradation of methylene blue as a test reaction was performed according to procedure reported the literaure.[31−33] Under both visible light ($\lambda > 420$ nm) and UV−visible light irradiation, samples TI and MTI show much better photocatalytic activity than P25. Furthermore, sample MTI is superior to sample TI in both cases (shown in Figure 9). The difference in photocatalytic activity between P25 and TI, MTI can be ascribed to the larger surface area of the latter (51 m^2 g^{-1} for P25 vs 118 m^2 g^{-1} and 157 m^2 g^{-1}) and additional high absorbance in the visible light range (between 420 and 550 nm). To understand the superiority of sample MTI with coexistence of anatase and rutile phases over the sample TI with full anatase phase, a detailed discussion is given below.

3.6. Discussion. From the above results, it can be seen that sample MTI with a bicrystalline framework of anatase and rutile shows much better photocatalytic activity than sample TI with pure anatase phase. It is known that the photocatalytic activity of titania is phase dependent. Anatase as a metastable phase exhibits the most active photocatalysis and the most stable rutile phase is less active or not active at all.[34,35] Our previous research also demonstrated higher photocatalytic activity for titania with lower ratio of rutile to anatase.[24] However, the above results are not obtained at similar conditions including crystal size, surface area, crystallinity, particle size, and morphology when the photocatalytic activity of anatase and rutile was compared. All these factors can greatly affect the photocatalytic activity of titania. In most cases, the available anatase titania is typically less than 50 nm in size. In contrast, the particle size for thermodynamically stable rutile phase is generally larger than 200 nm. Under this condition, the adsorptive affinity and capacity of anatase titania for organic molecules, O_2, surface water and hydroxyl are usually much stronger than that of rutile titania. The difference in the adsorptive affinity and capacity may intrinsically determine the photocatalytic activity of titania with different phase. So how about the photocatalytic activity for rutile titania with large surface area and small crystal size? In fact, the high photocatalytic activity has been obtained for the mesoporous rutile titania with a surface area of 174.5 m^2 g^{-1}.[36] Nitrogen-doped rutile titania with crystal size 9 nm and surface area 36 m^2 g^{-1} has also shown high photocatalysis.[19] It seems that crystal size and surface area can significantly affect the photocatalysis of rutile titania. This point can be partially proved by the fact that no obvious difference exists in the adsorptive capacity for surface water and hydroxyl between sample MTI with 43% rutile phase and the pure anatase TI (Figure 5).

The mixed-phase (anatase and rutile) titania and rutile itself with small size resulted in enhanced photocatalytic activity. A recent result demonstrated that rapid electron transfer, occurring from rutile conduction band to lower energy anatase lattice trapping sites in mixed-phase titania P25, leads to a more stable charge separation. The electron-transfer process causes the existence of catalytic hot spots at anatase/rutile interface.[37] However, this process is critically dependent on the small particle size of rutile phase and intimate contact between two phases.[37] The small size of rutile and intimate contact with anatase facilitate the electron transfer at the interface. In our case, rutile phase obtained was formed during hydrothermal treatment (100 °C) instead of calcination at high temperature. The crystal size of 16 nm of the rutile phase is relatively small and comparable to that of anatase phase (Table 1). From TEM images (parts C and D of Figure 4), it is clearly shown that disordered mesoporous structure is connected randomly and consisted of aggregated nanoparticles. It is expected that rutile and anatase phase can be in full contact. In other words, hot spots at the anatase/rutile phase interface can be active for sample MTI. Hong et al.[10] also prepared iodine-doped titania with mixed phases of anatase and rutile by calcinating the sample at 500 °C, which showed poor performance compared to iodine-doped anatase titania. The poor performance was due to the large rutile crystal size and the lack of intimate contact between two phases so that the mixed phases cannot demonstrate its structure advantage. On the other hand, it is well known that electron and hole pairs, generated in rutile titania with small particle size, possess much stronger redox ability than bulk rutile titania. This can also make photocatalysis more active in rutile titania itself. Furthermore, energetic electrons in the conduction band for small size rutile titania can be more effectively transferred into the lower energy lattice trapping sites of anatase. This process also slows the recombination of electron and hole pairs and improves photocatalysis in rutile. On the basis of the above consideration, it is important to control the rutile phase to small size in order to obtain high photocatalytic activity in the mixed-phase titania.

Many factors can affect the photocatalytic activity, so it is very difficult to estimate the contribution of each factor on the photocatalytic activity. For example, surface area and crystallinity usually appear to be two conflicting intrinsic properties of titania nanoparticles. Nonetheless, there is no doubt that large surface area contributes to high photocatalytic activity of titania nanoparticles with a certain crystallinity by creating more possible reactive sites on the surface of photocatalyst. Judging from XRD, Raman spectra and TEM image (Figure 4D), it can be seen that sample MTI has high crystallinity. Both large surface area and disordered mesoporous framework for the sample with high crystallinity can be accomplished by our current synthesis

Liu et al.

route. The disordered mesoporous structure is beneficial for promoting the diffusion of reactants and products, enhancing the photocatalytic activity by facilitating access to the reactive sites on the surface of photocatalyst. This point has also been demonstrated in Ni^{2+}-doped mesoporous titania for hydrogen production.[16]

The high absorbance from 400 to 550 nm for samples MTI and TI was attributed to iodine doping. However, to obtain high photocatalytic activity, it is vital to decrease the combination probability of the photoinduced electron hole pairs in photocatalyst. The superiority of MTI to TI in our case is attributed to the bicrystalline framework, large surface area, high crystallinity and mesoporous structure. With these characteristics of sample MTI, the separation of photoinduced electron hole pairs is favorable. After all, the separation of the electron hole pairs is responsible for photocatalytic activity.

4. Conclusions

MTI with a bicrystalline (anatase and rutile) framework was synthesized by a two-step template hydrothermal route. Its photocatalytic activity is compared with TI. The properties of samples TI and MTI were characterized by several techniques such as XRD, nitrogen adsorption and TEM, XPS, and UV−visible spectroscopy, Raman scattering, and FTIR. The superiority of sample MTI to TI in both the visible and UV−visible light range is attributed to its bicrystalline framework, high crystallinity, large surface area, mesoporous structure, and high absorbance in the visible light range by iodine doping. It is also found that the existence of rutile phase in titania has less effect on the adsorptive affinity and capacity of surface water and hydroxyl groups when rutile phase possesses comparable crystal size and surface area with anatase phase.

References and Notes

(1) Fujishima, A.; Honda, K. *Nature* **1972**, *238*, 37.
(2) Adachi, M.; Musuke Murata, Y.; Takao, J.; Jiu, J. T.; Sakamoto, M.; Wang, F. M. *J. Am. Chem. Soc.* **2004**, *126*, 14943.
(3) Linsebigler, A. L.; Lu, G. Q.; Yates, T., Jr. *Chem. Rev.* **1995**, *95*, 735.

(4) Aski, R.; Morikawa, T.; Ohwaki, T.; Aoki, K. *Science* **2001**, *293*, 269.
(5) Li, D.; Haneda, H.; Labhsetwar, N. K.; Hishita, S.; Ohashi, N. *Chem. Phys. Lett.* **2005**, *401*, 579.
(6) M.Khan, S. U.; AL-shahry, M.; Ingler, W. B., Jr. *Science* **2002**, *297*, 2243.
(7) Li, Y.; Hwang, D.; Lee, N. H.; Kim, S.-J. *Chem. Phys. Lett.* **2005**, *404*, 25.
(8) Ohno, T.; Tsubota, T.; Toyofuku, M.; Inaba, R. *Catal. Lett.* **2004**, *98*, 255.
(9) Ohno, T.; Akiyoshi, M.; Umebayashi, T.; Asai, K.; Mitsui, T.; Matsumura, M. *Appl. Catal. A: General* **2004**, *265*, 115.
(10) Hong, X.; Wang, Z.; Cai, W.; Lu, F.; Zhang, J.; Yang, Y.; Ma, N.; Liu, Y. *Chem. Mater.* **2005**, *17*, 1548.
(11) Lin, L.; Lin, W.; Zhu, Y. X.; Zhao, B. Y.; Xie, Y. C. *Chem. Lett.* **2005**, *34*, 284.
(12) ElShafei, G. M. S.; Philip, C. A.; Moussa, N. A. *Microporous Mesoporous Mater.* **2005**, *79*, 253.
(13) Peng, T.; Zhao, D.; Dai, K.; Shi, W.; Hirao, K. *J. Phys. Chem. B* **2005**, *109*, 4947.
(14) Yu, J. C.; Zhang, L.; Yu, J. *Chem. Mater.* **2002**, *14*, 4647.
(15) Yuan, S.; Sheng, Q.; Zhang, J.; Chen, F.; Anpo, M.; Zhang, Q. *Microporous Mesoporous Mater.* **2005**, *79*, 93.
(16) Jing, D.; Zhang, Y.; Guo, L. *Chem. Phys. Lett.* **2005**, *415*, 74.
(17) Yin, J. S.; Wang, Z. L. *Adv. Mater.* **1999**, *11*, 469.
(18) Wang, C.; Li, Q.; Wang, R. *J. Mater. Sci.* **2004**, *39*, 1899.
(19) Gandhe. A. R.; Naik, S. P.; Fernandes, J. B. *Microporous Mesoporous Mater.* **2005**, *87*, 103.
(20) Yu, J. G.; Yu, J. C.; Cheng, B.; Hark. S. K.; Iu, K. *J. Solid State Chem.* **2003**, *174*, 372.
(21) Spurr, R. A.; Myers, W. *Anal. Chem.* **1957**, *29*, 760.
(22) Kartini, I.; Menzies, D.; Blake, D.; Costa, J. C. D.; Meredith, P.; Riches, J. D.; Lu, G. Q. *J. Mater. Chem.* **2004**, *14*, 2917.
(23) Gregg, S. J.; Sing, K. S. W. *Adsorption, surface area and porosity*, 2nd ed.; Academic Press: London, 1982.
(24) Ding, Z.; Lu, G. Q.; Greenfield, P. F. *J. Phys. Chem. B* **2000**, *104*, 4815.
(25) Machado, N. R. C. F.; Santana, V. S. *Catal. Today* **2005**, *107−108*, 595.
(26) Ohno, T.; Tokieda, K.; Higashida, S.; Matsumura, M. *Appl. Catal. A: Chem.* **2003**, *244*, 383.
(27) Ivandaa, M.; Music, S.; Gotic, M.; Turkovic, A.; Tonejc, A. M.; Gamulin, O. *J. Mol. Struct.* **1999**, *480*, 641.
(28) Ohsaka, T. *J. Phys. Soc. Jpn.* **1980**, *48*, 1661.
(29) Choi, H. C.; Jung, Y. M.; Kim, S. B. *Vib. Spectrosc.* **2005**, *37*, 33.
(30) Bersani, D.; Antonioli, G.; Lottici, P. P.; Lopez, T. *J. Non-Cryst. Solids* **1998**, *175*, 232.
(31) Zhang, Q.; Gao, L. *Langmuir* **2004**, *20*, 9821.
(32) Mukai, S.; Nishihara, H.; Shichi, S.; Tamon, H. *Chem. Mater.* **2004**, *16*, 4987.
(33) Miyake, M.; Akachi, T.; Matsuda, M. *J. Mater. Chem.* **2005**, *15*, 791.
(34) Gerischer, H.; Heller, A. *J. Phys. Chem.* **1991**, *95*, 5261.
(35) Sato, S. *J. Phys. Chem.* **1983**, *87*, 3531.
(36) Li, Y.; Lee, N.-H.; Lee, E.-G.; Song, J. S.; Kim, S.-J. *Chem. Phys. Lett.* **2004**, *389*, 124.
(37) Hurum, D. C.; Agrios, A. G.; Gray, K. A.; Rajh, T.; Thurnauer, M. C. *J. Phys. Chem. B* **2003**, *107*, 4545.